Bi2O3/Nylon multilayered nanocomposite membrane for the photocatalytic inactivation of waterborne pathogens and degradation of mixed organic pollutants

View Article Online
View Journal

Environmental Science Nano

Accepted Manuscript

This article can be cited before page numbers have been issued, to do this please use: T. A. Gadhi, A. Qureshi, N. Channa, R. B. Mahar, A. Chiadò, C. Novara and A. Tagliaferro, *Environ. Sci.: Nano*, 2021, DOI: 10.1039/D0EN01026J.

View Article Online
DOI: 10.1039/D0EN01026J

Worldwide there is an increasing demand for clean water and sanitation systems and any different solutions are under evaluation, including advanced oxidation processes such as photocatalysis. This work describes the scalable synthesis process of an electrospun composite membrane made of Nylon and embedded α/β-Bi_2O_3 nanoparticles that can be activated by visible light instead of UV light typically used with other nanomaterials (e.g. TiO_2). As a proof of concept, the efficacy of the α/β-Bi_2O_3 electrospun composite membrane in the visible light inactivation of pollutants and pathogens was demonstrated in a Continuous-flow Photocatalytic Membrane Reactor, highlighting the great potential of this advanced photocatalytic process for clean water and sanitation.

Authors

Tanveer A. Gadhi[a], Aizaz Qureshi[a], Najeebullah Channa[a], Rasool Bux Mahar[a], Alessandro Chiadò[b*], Chiara Novara[b], Alberto Tagliaferro[b]

Affiliations

[a]U.S. Pakistan Center for Advanced Studies in Water (USPCASW), Mehran, University of Engineering and Technology, Jamshoro 76062, Pakistan.
[b]Department of Applied Science and Technology, Politecnico di Torino, Corso Duca degli Abruzzi 24, 10129 Torino, Italy.
*Corresponding Authors Email: alessandro.chiado@polito.it

Acknowledgements

The authors acknowledge the technical support of Prof. Zeeshan Khatri at the Mehran University of Engineering and Technology, Jamshoro, Pakistan, Prof. Jennifer Weidhaas at the University of Utah, USA, Prof. Paola Rivolo, and Dr. Pravin Jagdale from Politecnico di Torino, Italy, for their technical assistance. This study was financially supported by the United States Government and the American people through the United States Agency for International Development (USAID) and USPCAS-W, MUET research project funding. The contents are the sole responsibility of the authors and do not necessarily reflect the views of USAID or the United States Government.

View Article Online
DOI: 10.1039/D0EN01026J

Bi_2O_3/Nylon multilayered nanocomposite membrane for the photocatalytic inactivation of waterborne pathogens and degradation of mixed organic pollutants

Abstract

A powder semiconductor α/β- Bi_2O_3 was synthesized via solid state thermal annealing and further composited with a multilayered Nylon fibrous membrane via electrospraying. The successful integration of nano-sized α/β-Bi_2O_3 in the Nylon membrane was confirmed by XRD, FESEM images, UV-Vis, FT-IR and Raman analyses. The nanocomposite membrane displayed a visible-responsive catalytic ability with an energy bandgap of 2.78 eV estimated from the data of DRS. The activity of the composite membrane was examined in a continuous mode reactor for the degradation of separate and mixed solutions of anionic (Indigo Carmine) and cationic (Rhodamine B) organic pollutants. Moreover, the composite membrane exhibited antibacterial properties towards *E. coli*, a waterborne pathogen, as revealed by the obtained growth inhibition during Kirby-Bauer and in liquid culture tests. The inactivation of *E. coli* was confirmed by live/dead cell staining using fluorescence imaging. Finally, a mixed solution of organic dyes, as well as the recycle of the membrane and various concentrations of xenobiotics, showed the stability and potential of the α/β- Bi_2O_3 composite membrane for the removal of organic pollutants and inactivation of the waterborne pathogen.

Keywords: Bi_2O_3, Nanocomposite membrane, Wastewater, Photocatalysis, Antimicrobial, *E. coli*.

View Article Online
DOI: 10.1039/D0EN01026J

1. Introduction

Nowadays, there is an increasing demand for clean water and sanitation. One of the emerging technologies to get sustainable clean water can be based on advanced oxidation processes (AOP). Among them, the heterogeneous photocatalysis is an AOP process in which semiconductor materials are illuminated with solar/UV light to originate redox reactions and enable the treatment of organic, inorganic species, and microbes [1, 2]. However, its suitability in real applications is still challenged by various essential aspects. One of these is the cost-effective recovery of dispersed particles, their filtration and recycling [3-5]. Indeed, for high photoactivity, nano-scale particles are preferred because of prominent surface area, better dispersion in the bulk reactors, and optimum activation from the irradiation source [6, 7]. Though, these particles are hard to recover and reuse; moreover, they increase the operational cost of the water treatment [3, 4]. Alternatively, various studies have suggested diverse materials as fixed supports for the active particles, with a focus on carbon, silica, and mineral-based porous supports that could allow a good contact between the immobilized semiconductors and the targeted contaminant for continuous treatment. Examples of such supports are silica-based [8-10], activated carbon [11, 12], synthetic clay laponite [13], glass, steel mesh [14-16], and recently some polymers such as polyimide [17]. However, with such immobilized fixed supports, the photocatalytic response is reportedly lower than using bulk materials, because of low dispersion, reduced transparency, limited mass transfer, and weak interaction of the immobilized semiconductor with the targeted contaminants [3]. Thus, these limitations slower the advancement of non-slurry application alternatives, as the immobilization supports should satisfy requirements of chemical inertness, transparency to the irradiation source, and adequate channels and permeations to capture the targeted contaminants in the bulk reactors [18, 19].

View Article Online
DOI: 10.1039/D0EN01026J

Merging membrane and photocatalytic technologies has been considered recently. In this case the semiconductor materials could be incorporated/embedded within the porous membrane to maximize the degradation efficiency. Such an approach turned into a great achievement in treating wastewater. The porous network of tiny channels in the membrane could be used to embed the semiconductor materials, and further to capture and adsorb the contaminants, so as their removal could be maximized. Recent results have shown that adding semiconductor particles to the membrane has improved water flux [20], refined permeability and selectivity [21], boosted antifouling properties [22] and raised adsorption sites, which ultimately enhanced the adsorption of the membrane [23]. Different kinds of materials were used to prepare photocatalytic membranes such as ceramics, zeolites, but mostly polymers [24]. However, irradiation and generation of oxidizing species in the reaction environment cause abrasion and leaching of the semiconductor from the membrane itself [24]. Therefore, for its chemical, thermal, and mechanical stability, Nylon polymer could be a promising option for semiconductor embedding and composite usage as a photocatalytic membrane. Indeed, electrospun Nylon-6 nanofibers have a large surface area and active sites that could improve the adsorption of pollutants for the subsequent degradation [25]. Moreover, the electrospun nanofibers have demonstrated improved properties in dye removal [26], advanced filtration [27], and antibacterial properties [28].

Besides the degradation and removal of organic and inorganic pollutants, various studies have explored the potential of semiconductor-polymeric composite membranes for the inactivation and removal of pathogens through the same principle i.e. the attack of the cell membrane through reduction-oxidation reactions and consequently the reduction in their growth [28, 29]. Some of the reported semiconductor composite membranes include embedded oxides of silver, titanium, cerium, zirconium, and iron, and have shown antimicrobial response against common pathogens

View Article Online
DOI: 10.1039/D0EN01026J

i.e. *Escherichia coli*, *Staphylococcus aureus*, *Enterococcus sp., Pseudomonas aeruginosa*, *Klebsiella pneumonia* [30-33]. Amongst various semiconductors, the bismuth-based materials, such as $BiVO_4$ [34], Bi_2O_3 [35, 36], BiOX(Cl, I, Br) [37], and bismuth-based composites [38, 39], have been proven efficient in water treatment due to their ability to produce Reactive Oxygen Species (ROS). Among them, Bi_2O_3 has emerged as the most effective visible light-responsive material with promising optical, electrical, thermal, and photocatalytic properties [40]. Moreover, it also has a tunable bandgap between 2.1 to 2.8 eV compared to 3.2 eV of TiO_2. The solar light viable bandgap is a result of the Bi_2O_3 hybrid valence band arising from contributions of Bi 6s and O 2p orbitals; in contrast, the TiO_2 valence band only has O 2p orbitals contributions [41].

To the best of our knowledge, Bi_2O_3-polymeric nanocomposite membranes have rarely been investigated against the removal of both organic pollutants and waterborne pathogens. Therefore, this study was conducted to exploit and investigate the potential of Bi_2O_3 integration in a Nylon-6 membrane. Once synthesized, the membranes were characterized by XRD, FESEM, UV-Vis, FT-IR and Raman analyses, to check the proper integration of the α/β- Bi_2O_3 nanomaterials in the Nylon membrane. Afterward, the degradation efficiency of the composite membranes against single and mixed solutions of anionic (Indigo Carmine) and cationic (Rhodamine-B) organic dye pollutants and against a pathogenic strain of *E. coli*, was evaluated by using a Continuous-flow Photocatalytic Membrane Reactor (CPMR), paving the way for a new approach in getting water purification.

2. Experimental section

2.1 Materials and chemicals

Nylon-6 pellets (density of 1.084 g/mL), formic acid, ethanol, polyethylene glycol (PEG), Triton-X, bismuth (III) nitrate pentahydrate ($Bi(NO_3)_3{:}5H_2O$) and Indigo Carmine (IC), Rhodamine B

View Article Online
DOI: 10.1039/D0EN01026J

(RhB), were purchased from Sigma Aldrich, Italy. Sodium chloride (NaCl) was purchased from Daejung Co. Ltd., Korea. The bacterial culture media (agars and broths) were purchased from Oxoid, England. For the live/dead cells staining, a LIVE/DEAD® BacLight™ Bacterial Viability Kit was purchased from ThermoFisher Scientific, USA; this kit included two staining dyes, SYTO-9 and Propidium Iodide (PI), at 20 mM concentration each. All the materials and chemicals were used as received.

2.2 Synthesis of α/β-Bi_2O_3

The α/β-Bi_2O_3 powder was synthesized from $Bi(NO_3)_3{:}5H_2O$ solid thermal annealing route. The synthesis details are published elsewhere [42]. In brief, the measured quantity of $Bi(NO_3)_3{:}5H_2O$ was placed in a ceramic crucible and directly heated inside the muffle furnace at an initial temperature of 150 °C for 30 min. Afterward, the temperature was raised to 250 °C and kept constant for 2 h, and finally, the temperature was increased to 550 °C for 45 minutes to obtain the α/β-Bi_2O_3 composite. This composite (in bulk form) was already reported as a visible-responsive semiconductor for the degradation of organic compounds [42].

2.3 Preparation of Bi_2O_3/Nylon composite membrane

The obtained α/β-Bi_2O_3 powder 10wt.% was dissolved in ethanol. Measured drops of PEG and Triton-X were gradually added in the ethanol mixture at continuous mixing i.e. to ensure well-segregated particle suspension and homogenization. The obtained solution was stirred for 18 hours and then sonicated for 30 minutes to get a homogeneous yellow colored solution. The Nylon-6 solution was made by dissolving 22 wt.% Nylon pellets in formic acid, by stirring it continuously at 100 rpm for 6 hours to produce a neat and transparent Nylon-6 solution. Then, the Nylon-6 solution was electrospun to produce a multilayered nylon fibrous membrane. The multilayers referred to the electrospun and stacked fibrous layers of Nylon that overlaid one after one. The

View Article Online
DOI: 10.1039/D0EN01026J

applied voltage was altered between 18 and 24 kV to obtain thick and ultra-thin spiderweb type multilayered nano-fibers [43]. The injection flow rate was set to 0.95 mL/h at a 12 cm tip to collector distance. Electrospinning was followed by electrospray of α/β-Bi_2O_3 solution on the surface of the obtained Nylon electrospun multilayers i.e. for successful integration of α/β-Bi_2O_3. Fig. 1 depicts the scheme of the electrospinning process for the preparation of bare and α/β-Bi_2O_3 composite membranes and the digital image of obtained membrane. The obtained membranes were referred to as bare-Nylon and Bi_2O_3/Nylon composite. Visually, the surface of the obtained Bi_2O_3/Nylon membrane showed a homogeneous pale-yellow non-dusty appearance as an indication of the embedded Bi_2O_3 particles.

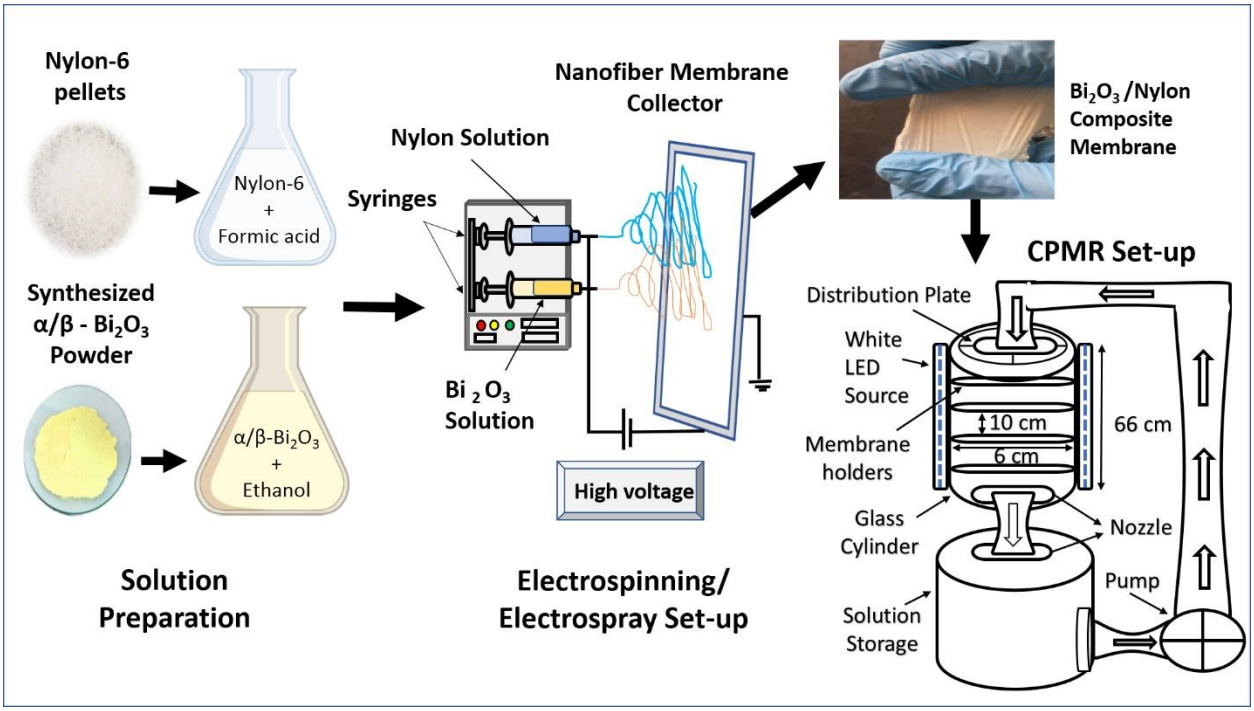

Figure 1 Schematic layout of membrane preparation and photocatalytic tests.

2.4 Characterization of the bare and composite membrane

To observe and analyze the microstructure and morphology of the obtained bare and composite membranes, an in-lens detector of a Zeiss Supra 40 Field Emission Scanning Electron Microscope

View Article Online
DOI: 10.1039/D0EN01026J

(FESEM) was used to acquire secondary electron contrast images with 5 keV electrons (Zeiss SMT, Oberkochen, Germany). An Energy-Dispersive X-Ray Spectroscopy (EDX) analysis was performed during FESEM imaging. To this aim all the peaks were used for the elemental analysis (3 iterations), that was carried out with 15 keV electrons. To analyze the size and phase composition of the obtained membranes, Panalytical X'Pert MRD Pro Cu Kα X-ray source in Bragg/Brentano configuration was used. The sample was scanned at a 2θ range of 20-60°. A Varian Cary 500 spectrophotometer equipped with an integration sphere was used to record the diffuse reflectance spectroscopy (DRS) and transmittance spectra of the bare and composite membranes. Tauc plots of the Kubelka Munk function were used to calculate the energy bandgap (E_g) value. The FT-IR analysis was performed in Attenuated Total Reflection (ATR) mode to identify the chemical changes in the membrane after the incorporation of α/β-Bi_2O_3. The spectra were collected with a 4 cm^{-1} resolution by accumulating 64 scans each spectrum on a Nicolet 5700 FTIR Spectrometer (Thermo Fisher) equipped with a diamond crystal and a DTGS detector (at room temperature) in the 400–4000 cm^{-1} range. Raman spectra were acquired with a 785 nm laser source using an InVia Qontor Raman microscope (Renishaw plc, Wotton-underEdge, UK) equipped with a 20x objective, in backscattering configuration. The output laser power was attenuated to 25 mW and the acquisition time was 50 s.

2.5 Photocatalytic evaluation

2.5.1 Continuous-flow photocatalytic membrane reactor (CPMR)

Fig. 1 shows the schematic diagram of the in-house fabricated CPMR for the evaluation of the efficacy of the membranes on selected dyes and bacteria. The CPMR includes a cylindrical tube made of borosilicate glass with four membrane holders (each 6 × 6 cm) for placing the prepared membrane in a straight position at a distance of 10 cm form each other. A white LED light source

View Article Online
DOI: 10.1039/D0EN01026J

for the activation of integrated α/β-Bi_2O_3, with a measured irradiance of around 70 W/m^2 (at the cylinder's center of all positioned membranes) and an emission spectrum between 400-700 nm, was attached outside of the cylinder. Beneath the cylindrical tube, the storage tank was connected via a peristaltic pump i.e. for the circulation of stock solution (2 L) over the membrane (i.e. inside the cylindrical tube) at a constant flow of 25 mL/min. For dark conditions, the LED light remained switched-off; besides, aluminum foil was wrapped on the cylindrical tube.

2.5.2 Photocatalytic discoloration tests

Anionic IC and cationic RhB dyes were selected as model pollutants because of their common use in photocatalytic evaluation [42]. For the preliminary experiments, both dyes were tested separately at a concentration of 5 ppm. Initially, to achieve adsorption/desorption equilibrium, the LED lights remained switched-off for the first 30 minutes. Afterward, the solution was irradiated to analyze the photocatalytic removal and assess the degradation kinetics. 3 mL of the samples were collected in a predefined time sequence of photocatalytic treatment, centrifuged for 5 minutes for the analysis, and afterward returned to the stock solution to avoid any interference to the system kinetics. The centrifuged samples were analyzed using a double beam UV-Vis spectrophotometer (Perkin Elmer-LAMBDA 365) for recording the time-dependent intensity reduction and changes in the absorbance spectra of the model pollutants. For the mineralization degree of the treated dye solutions, total organic carbon (TOC) analysis was carried using the TOC-L SHIMADZU TOC analyzer. For TOC analysis, the control and the treated samples of both dyes were collected and analyzed using the protocol reported in the literature [44]. The stability of the membrane was evaluated by testing the same membrane up to three cycles using the IC solutions at a fixed concentration of 5 ppm. Before reuse, the recovered membranes were thoroughly rinsed with distilled water.

View Article Online
DOI: 10.1039/D0EN01026J

For the composite membrane performance against the mixed regime of dyes, i.e. of different chemical structures and ionic behaviors, separately prepared solutions of IC and RhB (at a molar concentration of 1 x 10^{-6} M) were mixed at even proportion. The prepared mixed stock of 2 L was evaluated on the CPMR, under similar operating conditions, briefed earlier.

2.5.3 Photocatalytic bacterial inhibition/inactivation

Initially, the inhibition of *E. coli* ATCC (8739) was performed on agar plates, using the bare and composite membrane cut into 10 x 10 mm^2 pieces. In brief, the inoculum (100 µL) was taken from the overnight incubated *E. coli* culture at the concentration of 1x10^6 CFU/mL and was spread on LB agar plates. Then, the bare Nylon/composite membrane was placed in the center of the plate and incubated for 24 h at 37 ± 1 °C; the test was performed in the dark or in the presence of white LED lamp (100 W/m^2). After 24 hours, the inhibition zone was observed in the culture plates [45]. The experiments were conducted in duplicate, and the zone of inhibition was calculated as suggested in the previously reported studies [46, 47]. Further, for the evaluation of liquid bacterial suspension, *E. coli* was inoculated in a 50 mL tube of LB broth (Oxoid, England) after overnight incubation at 37 °C and shaking at 120 rpm. Afterward, the culture broth was centrifuged at 5000 rpm for 10 minutes, and the settled pellets were washed several times with a sterilized normal saline solution (0.85% of NaCl). Then, the bacterial biomass was diluted in 2 L of saline solution to reach a bacterial concentration around 1x10^6 CFU/mL, by measuring an optical density (OD) of 0.01 at 600 nm. The prepared bacterial stock was tested in the CPMR for photocatalytic inactivation, at 25 mL/min. Initially, the dark conditions were maintained for 30 minutes, then the cylindrical tube was irradiated. A 100 µL sample was collected in a predefined time sequence of photocatalytic treatment. The collected samples were serially diluted and plated on LB agar plates, incubated for 24 hours at 37 °C, and the numbers of bacterial colonies were counted.

View Article Online
DOI: 10.1039/D0EN01026J

To observe if the photocatalytic action was able to damage the *E. coli* cells, live/dead bacterial cell fluorescence staining was performed. For this, a 1 mL sample was collected at different time intervals, centrifuged at 10,000 rpm for 15 minutes, and then the bacterial biomass was washed with sterilized saline solution. Finally, the obtained bacterial biomass was resuspended in 1 mL of sterilized saline solution. Afterward, by following the protocol provided in the received live/dead fluorescence staining kit, a 1:1 mixed dye stock solution of SYTO-9 (3.34 mM, excitation 483 nm, emission 503 nm) and Propidium iodide (PI; 20 mM, excitation 535 nm, emission 617 nm) was prepared. For the fluorescence microscope imaging, 5 µL of the mixed dye stock solution was added in the bacterial suspension and incubated in the dark for 30 minutes. After incubation, 5 µL of the stained bacterial suspension was collected and pipetted over a glass slide and covered for fluorescence analysis. The fluorescence microscope (Zeiss Axio Scope.A1, Carl Zeiss, Germany) equipped with FITC and Texas RED filters, was used to acquire fluorescence images. The acquired images were analyzed via ImageJ 1.50d to assess the percentage of live (green-stained) and dead (red-stained) bacterial cells.

3. Results and discussions

3.1 Characterization

The composite membranes containing the bismuth oxide-based nanomaterial were synthesized and characterized, as described in the experimental part. In the following, the physical-chemical characterization using XRD, UV-Vis, FT-IR, Raman spectroscopy, FESEM imaging, EDX analysis are reported.

3.1.1 XRD analysis

The XRD patterns of bare Nylon, Bi_2O_3/Nylon, and synthesized α/β-Bi_2O_3 powder are shown in Fig. 2A. The bare Nylon, being semi-crystalline, does not show any peak, while in case of

View Article Online
DOI: 10.1039/D0EN01026J

Bi_2O_3/Nylon composite some peaks were observed at 27.06°, 31.7°, and 53.6° indicating the formation of monoclinic α- Bi_2O_3 phase [42]. These peaks match with standard XRD data (JCPDS 16-0654) [43]. Additional peaks were observed at 2Θ = 27.96, 32.72°, and 46.22°, corresponding to β-Bi_2O_3 phase (JCPDS card no. 01-078-1793) [42]. As shown by the comparison in Fig. 2A, the pattern of the Bi_2O_3/Nylon composite retained the main peaks observed for the α/β-Bi_2O_3 powder after integration into Nylon by electrospinning. However, due to the dilution in the Nylon membrane, the weaker peaks of the XRD spectra of α/β-Bi_2O_3 could not be detected [48].

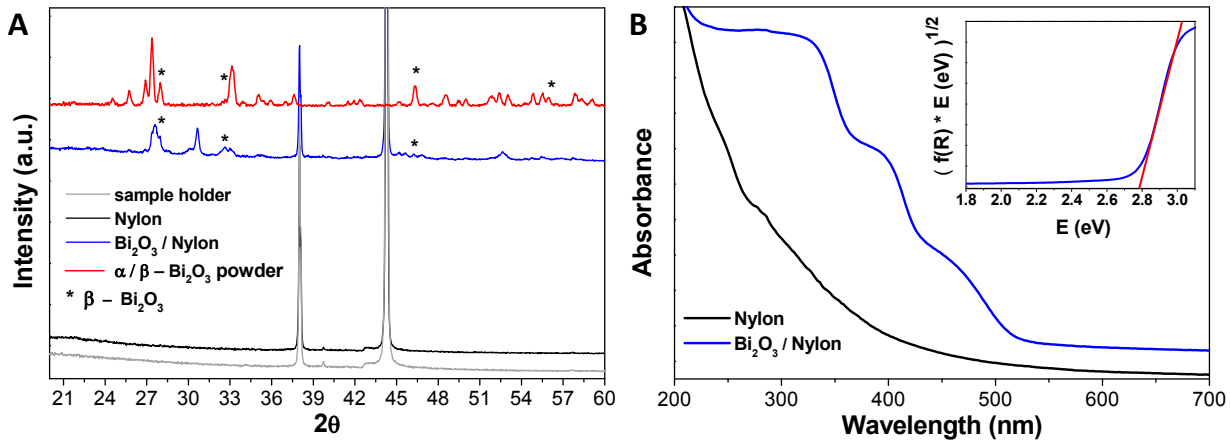

Figure 2 A) XRD patterns of the sample holder, bare Nylon, Bi_2O_3/Nylon composite, and synthesized α/β- Bi_2O_3 powder, and B) UV-Vis DRS Spectra of bare Nylon, Bi_2O_3/Nylon composite; inset Tauc plot for the estimation of the bandgap.

3.1.2 Optical properties

Fig. 2B shows the DRS spectra of the bare and composite Nylon membranes. The bare Nylon displayed a slight absorption in the region 250 nm to 300 nm, typical of Nylon polymer [49]. Instead, the Bi_2O_3/Nylon composite membrane exhibited one absorbance stretch in the plateau between 375 nm and 450 nm, which is the characteristic optical transition range of α-Bi_2O_3. Moreover, an extended absorbance stretch in the range of 450-530 nm represented the characteristic transition range of β-Bi_2O_3 [42]. The observed adsorption edge in the visible

View Article Online
DOI: 10.1039/D0EN01026J

spectrum could facilitate the transition of the electrons from the valence to the conduction band and consequently allow the composite membrane to harvest the solar irradiation for photocatalytic activity [34]. The bandgap of the composite membrane estimated from the Tauc plot was around 2.78 eV i.e. shown in inset Fig. 2B. As per the XRD analysis, the α-phase is dominant in the α/β-Bi_2O_3 composite. Therefore, the two absorption edges in the visible region have a combined representation in the Tauc plot, and the predominant characteristics of α-Bi_2O_3 were slightly narrowed due to the presence of β-Bi_2O_3.

3.1.3 FESEM analysis

Fig. 3 shows the FESEM images of bare Nylon (Fig. 3A, 3B) and Bi_2O_3/Nylon composite (Fig. 3C, 3D) at different magnification. In the case of bare Nylon, the images exhibited both thick and thin electrospun nanofiber strands in the range of 20-60 nm diameter that form a net-like structure with overlaid multilayers [43, 50]. The obtained nanofibers displayed a uniform and bead-free formation. In the case of the Bi_2O_3/Nylon composite, the FESEM images in Fig. 3C shows the integration of nano-sized round Bi_2O_3 particles over the Nylon fibers. Moreover, Fig. 3D suggests that this integration was achieved across each electrospun layer and in the whole thickness of the membrane.

View Article Online
DOI: 10.1039/D0EN01026J

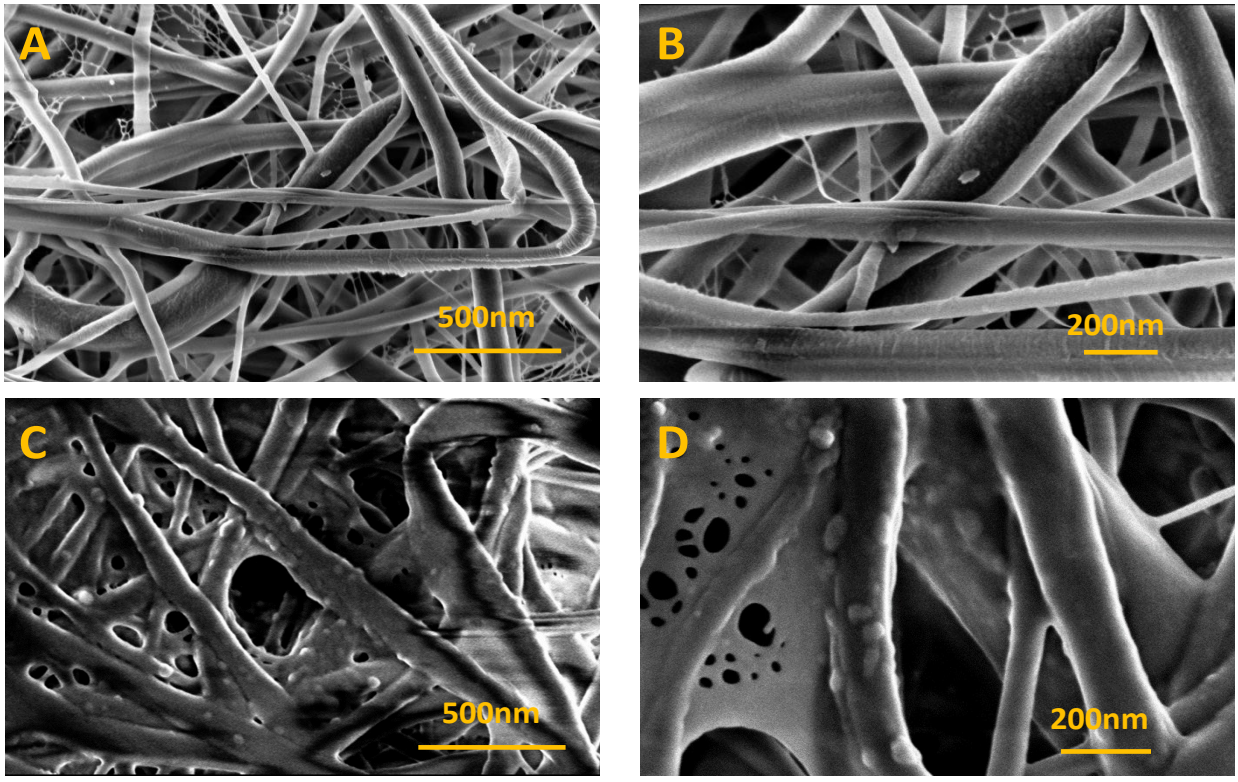

Figure 3 FESEM images of bare Nylon and Bi_2O_3/Nylon membranes at different magnifications. (A) bare Nylon (25 kX), (B) (50 kX), (C) Bi_2O_3/Nylon (25 kX), and (D) (50 KX).

A further confirmation of the integration of the bismuth nanomaterial into the multilayered electrospun membrane was revealed by the EDX analysis, reported in Fig. S1. This evaluation clearly revealed the presence of Bi atoms in the Bi_2O_3/Nylon membranes.

3.1.4 FT-IR analysis

Fig. 4 shows the FT-IR spectra of the bare and composite membranes samples. Nylon-6 is a polyamide, therefore, its molecular structure is featured by the presence of amide groups as displayed by the amide I stretching at 1638 cm^{-1} (C=O stretching), and amide II stretching at 1540 cm^{-1} (as a combination of -CN stretching and -NH bending) [51]. At the same time, the intense band at 3297 cm^{-1} indicates the N–H stretching vibration [52]. The peaks at about 1367 cm^{-1}, 1263 cm^{-1}, and 1200 cm^{-1} are due to amide III stretching and CH_2 wagging, while the peaks at 2860 cm^{-1}

View Article Online
DOI: 10.1039/D0EN01026J

and 2933 cm^{-1} are due to CH_2 symmetric and asymmetric stretching, respectively [52]. All other peaks match with FT-IR assignments of Nylon-6 nanofibers reported previously and summarized in Table S1 [51, 52]. In the Bi_2O_3/Nylon composite, concerning Bi_2O_3, its leading bands are below 500 cm^{-1}, but the ATR diamond crystal used to acquire the spectra cuts this region. The only clear signal of bismuth oxide is the peak at 846 cm^{-1} due to the symmetric Bi-O stretching [53]. Nevertheless, some of the absorption bands of Nylon-6 are downshifted. In particular, the amide I and amide II bands are shifted to 1635 cm^{-1} and 1538 cm^{-1}, respectively, whereas the N–H stretching is moved to 3294 cm^{-1}. This is probably the result of the interaction of the Nylon polymer with Bi_2O_3.

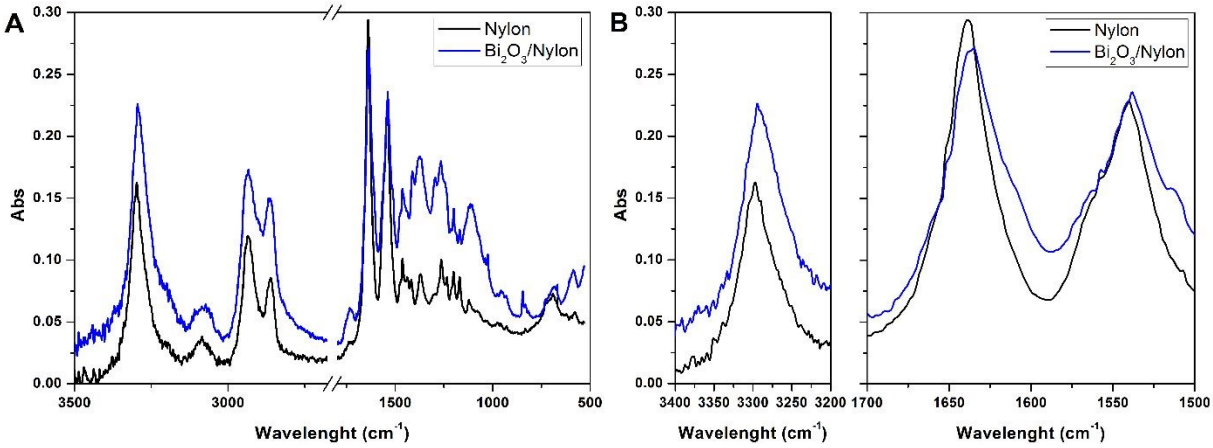

Figure 4 FT-IR Patterns of Nylon and Bi_2O_3/Nylon membranes: A) whole FT-IR spectrum b) magnification of the N-H stretching (left) and amide I and amide II (right) regions.

3.1.5 Raman analysis

Raman analysis of the bare Nylon and composite membranes was performed to further assess the incorporation of the α/β–Bi_2O_3 nanoparticles. As shown in Fig. 5 the Nylon fibers are featured by a weak Raman signal that matches the typical vibrational pattern of polyamides.

View Article Online
DOI: 10.1039/D0EN01026J

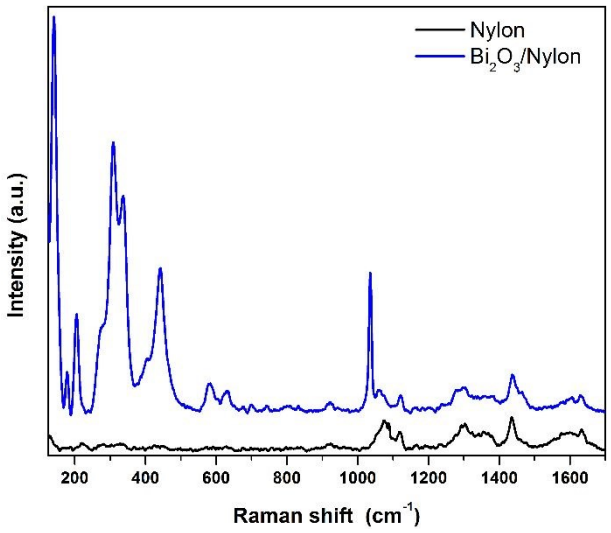

Figure 5 Raman spectra of the bare (bottom black curve) and α/β -Bi_2O_3 decorated (top blue curve) Nylon membrane.

In detail, different bands assigned to CC stretching coupled to CH_2 bending modes are observed around 1100 cm^{-1} (CC stretching + CH_2 twisting around 1080 and CC stretching + CH_2 wagging at 1120 cm^{-1}), while two CH_2 twisting and one CH_2 bending-related bands are detected between 1260-1300 cm^{-1} and at 1440 cm^{-1}, respectively [54]. Finally, amide I band appears at about 1635 cm^{-1} [55]. The addition of the Bi_2O_3 nanopowder results in significant changes in the low Raman shift range, while the vibrational pattern is almost unaffected over 600 cm^{-1}, except for a narrow band at 1040 cm^{-1} due to residual nitrates from the synthesis. The emergence of intense Raman modes in the 120-600 cm^{-1} range attributable to two different Bi_2O_3 crystalline phases clearly witness the incorporation of the bismuth oxide in the membrane. The bands at 278, 313 and 440 cm^{-1} were previously assigned to α-Bi_2O_3 [56, 57]. Instead, the vibrational modes at 142 and 335 cm^{-1} appear slightly up-shifted with respect to the main bands of the β-Bi_2O_3 (128 cm^{-1} and 317 cm^{-1}) [58], but can still be consistent with the presence of the tetragonal phase. Depending on the Raman shift region where they occur, the observed Raman bands can be attributed to Bi-dominated lattice movements (< 155 cm^{-1}), modes with significant Bi and O contribution (155-255 cm^{-1}) and

View Article Online
DOI: 10.1039/D0EN01026J

oxygen related displacements (> 255 cm^{-1}), as derived previously for α-Bi_2O_3 [57]. Raman analysis thus confirms both the formation of the composite and the preservation of the crystalline phases of the nanopowder after electrospinning.

3.2 Photocatalytic dye discoloration/degradation

Once the composite membranes have been physico-chemically characterized, their photocatalytic efficiency was evaluated, employing photocatalytic tests against anionic IC and cationic RhB organic dyes. The selection of these dyes was made to compare the obtained results with the previously reported ones, in which both dyes were evaluated individually and in a mixed solution using the bulk α/β-Bi_2O_3 powder [42].

3.2.1 Indigo carmine (IC) dye

View Article Online
DOI: 10.1039/D0EN01026J

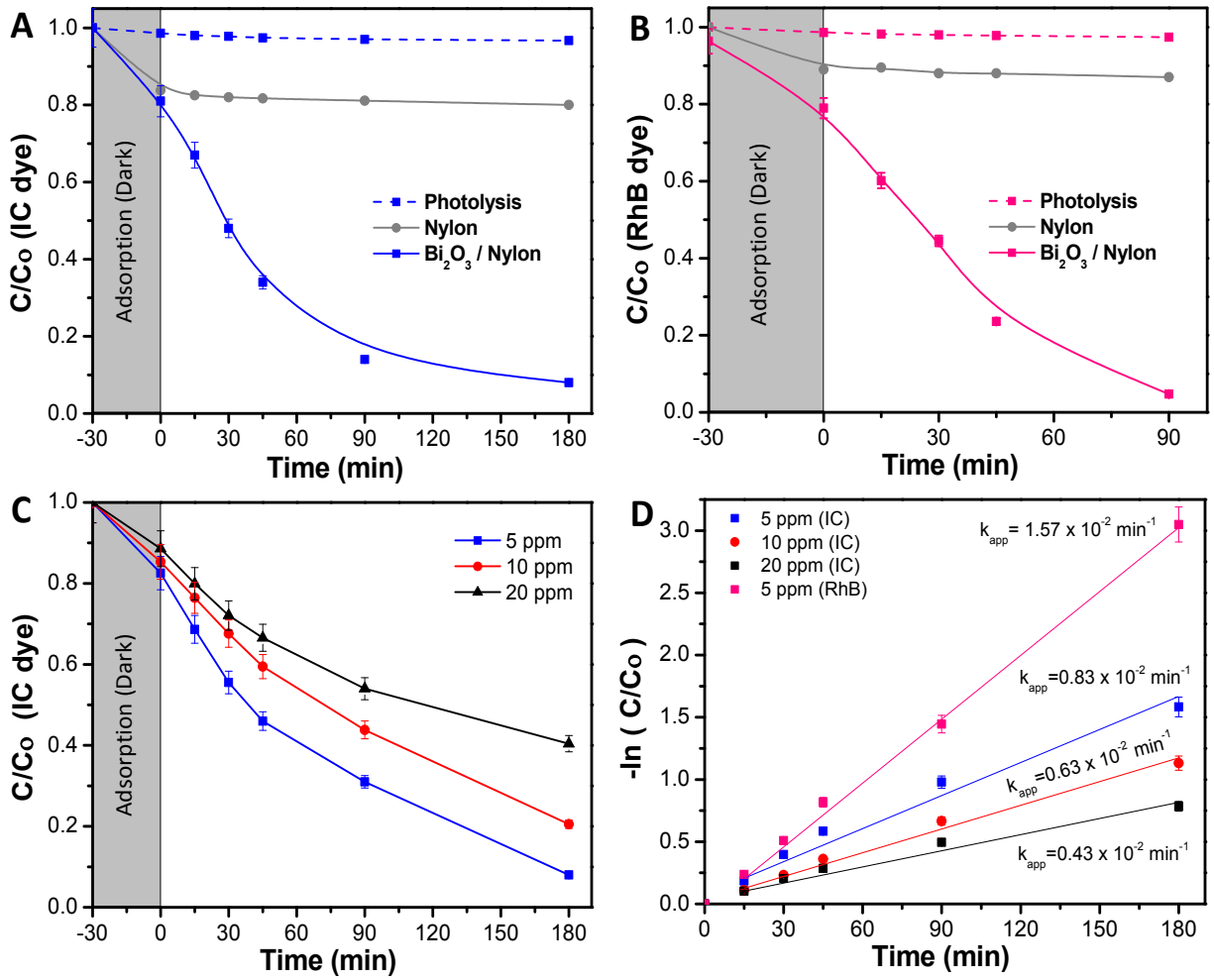

Figure 6 Photocatalytic tests using bare Nylon and Bi_2O_3/Nylon composite membranes: A) Relative concentration (C/Co) of IC degradation vs time (Co = 5 ppm); B) C/Co of RhB degradation vs time (Co = 5 ppm); C) C/Co of different IC dye concentrations with Bi_2O_3/Nylon composite membrane, and D) Kinetic curve of IC and RhB dye solutions, and estimated apparent kinetic rates (K_{app}).

Fig. 6A shows the relative concentration (C/C_o) profile of IC dye at different times of photocatalytic exposure, using bare Nylon and Bi_2O_3/Nylon composite membranes. The absorption spectra of IC *vs* different treatment time using Bi_2O_3/Nylon is given in Fig. S2 of supplementary data. Initially, in the dark condition, the absorbance spectra of IC dye at 610 nm was reduced by 21.4% due to its charge interactions towards the Nylon multilayers [59]. Any

View Article Online
DOI: 10.1039/D0EN01026J

further decrease due to adsorption was not observed for a longer period in the dark. Instead, after the irradiation exposure, the absorbance peak of IC started to decrease further, due to the photocatalytic response of the α/β- Bi_2O_3, until it completely disappeared after prolonged exposure of 180 minutes. The removal of IC is due to the oxidation and breaking of the indigoid group (NHC=CNH), as indicated by the observed isosbestic point at 250 nm and by the increase of absorbance of intermediate products (shown in Fig. S2) i.e. *Isatin sulfonic acid* and *2-amine-5-sulfo-benzoic acid*, in the UV absorbance region between 250 nm and 275 nm [5, 42]. The persisted appearance of these peaks was probably the indication of incomplete mineralization [44].

Further, in Fig. 6A the photolysis of IC dye solution i.e. under irradiation exposure without the presence of any membrane showed no/less significant change in the IC concentration, while in the case of bare Nylon membrane, around 19% of IC dye was initially adsorbed in the dark conditions and, afterward, did not show any further activity in the light. This could be ascribed to a limited amount of adsorption sites of the Nylon fibrous membrane, which could not accommodate further dye molecules, resulting in a limited removal of the dye from the solution [26]. Instead, the Bi_2O_3/Nylon composite membrane showed slightly higher adsorption (21.4%), compared to the bare Nylon membrane. This could be related to additional adsorption sites provided by the embedded nanoparticles [23]. Afterward, in the following first 45 min of irradiation, the improved removal of IC was observed due to the high concentration of adsorbed IC molecules over the membrane surface, which was rapidly oxidized by the generated ROS after irradiation. Further, after 180 min of irradiation, around 78% of mineralization was achieved, as analyzed by the TOC analysis. Afterward, the TOC reduction remained unchanged for a longer run of 360 min, due to the persistent nature of the resulted intermediates [42]. The kinetic curve for the degradation of IC (shown in Fig. 6D; at 5 ppm concentration) is plotted using the ln (C_o/C) function vs time that

View Article Online
DOI: 10.1039/D0EN01026J

resulted in a straight line ascribed to pseudo-first-order reaction [44], with a calculated apparent kinetic rate (K_{app}) of 0.83×10^{-2} min^{-1}.

3.2.2 Rhodamine B (RhB) dye

RhB is a cationic dye and has both diethylamine and carboxylic groups [42]. Fig. S3 in the supplementary data shows the UV-Vis absorbance spectra of RhB at different time intervals obtained with Bi_2O_3/Nylon composite membrane. The RhB shows the maximum absorbance peak at 555 nm [40], which was followed to relate its removal via simultaneous adsorption and photocatalytic oxidation. In Fig. 6B, C/C_o profiles of RhB dye at different times of photocatalytic exposure, using bare Nylon and Bi_2O_3/Nylon composite membranes are compared. Initially, 21% of the RhB intensity was reduced due to its interaction with the multilayers and integrated Bi_2O_3 particles i.e. under dark conditions, and the adsorption-desorption equilibrium was attained with the saturation of the composite membrane by RhB dye molecules as no further adsorption noted up to 60 min in dark conditions. The interaction of cationic dyes with Nylon is assumed to be weaker than that of anionic dyes. However, an improved interaction of RhB dye with the composite membrane was observed. This could be associated with the anionic carboxylic group of RhB and good protonation of α/β-Bi_2O_3 particles that could have allowed amphoteric sites of RhB to interact with the composite membrane [42]. After the irradiation, the adsorbed and highly interacting RhB dye was removed and oxidized by the reactive species generated by the composite α/β-Bi_2O_3 particles after 90 minutes, and reached a degradation and mineralization degree up to 68% after 180 min exposure, as observed through TOC analysis. The mineralization of RhB was unchanged after that due to the formation of persistent intermediates [44]. Compared to IC dye, the removal of RhB was found faster with the calculated K_{app} of 1.57×10^{-2} min^{-1} i.e. shown in Fig. 6D. The improved kinetics of RhB could be due to its high affinity towards the membrane and

View Article Online
DOI: 10.1039/D0EN01026J

the close interaction with the ROS originated by the composite α/β-Bi_2O_3 particles. Moreover, Fig. 6B showed no significant change in the RhB concentration in the case of treatment with bare Nylon membrane, under photolysis conditions.

3.2.3 Varied dye concentrations

To evaluate the membrane performance at high loading of the IC dye, the photocatalytic tests were conducted at varied IC concentrations using the Bi_2O_3/Nylon composite. Fig. 6C and 6D show the C/C_o and removal kinetics of IC at the concentrations of 5, 10 and 20 ppm, and reveal that the removal efficiency of the Bi_2O_3/Nylon composite membrane decreased to 75.11%, and 61.45% at the concentrations of 10 and 20 ppm, respectively, during 180 minutes irradiation exposure. This behavior could be related to the low availability/generation of ROS due to the attachment of the dye molecules on active sites of α/β-Bi_2O_3. Secondly, the resulting increase in solution opacity and consequently the decreased irradiation transmission subsequently lowered the removal efficiency of IC [60, 61]. Moreover, the high organic load could reduce the water flux and increase the mass transfer resistance of the membrane and could decrease the membrane efficiency [62]. This trend was observed during the TOC analysis, which revealed a decrease in the degradation and mineralization efficiency of the composite membrane, i.e. after 180 min irradiation, the analyzed TOC reduction was 63% and 37% for 10 and 20 ppm concentrations of IC dye, respectively, compared to 78% reduction in case of 5 ppm solution. The resultant decrease in mineralization efficiency could be due to the saturation of the composite membrane with intermediate species that affected the semiconductor activation to support the generation of reactive species and induce oxidation. The Fig. 6D, shows calculated K_{app} values as 0.63×10^{-2} min^{-1} and 0.43×10^{-2} min^{-1} for 10 and 20 ppm IC dye concentrations, significantly reduced compared to 0.83×10^{-2} min^{-1} in the case of 5 ppm concentration.

View Article Online
DOI: 10.1039/D0EN01026J

3.2.4 Mixed dyes degradation

Since colored wastewater contains the mixture of several dyes, interfering with each other in the mixed effluent, their removal behavior and mechanism of interaction for any potential treatment (including the case of membrane assisted photocatalysis) could be different. Therefore, the evaluation of a mixed solution of both IC and RhB dyes was performed using the composite membrane. The recorded absorbance spectrum of the mixed solution *vs* irradiation time given in Fig. 7A showed two main peaks corresponding to the contribution of both IC and RhB dyes at 610 and 555 nm, respectively. In Fig. 7B, C/C_o profile of mixed solution at different times of photocatalytic exposure are reported i.e. using bare Nylon and Bi_2O_3/Nylon composite membranes.

In dark conditions, both IC and RhB dyes preferentially adsorbed on the membrane at 23% and 22%, respectively. After irradiation, the absorbance of the IC dye was significantly reduced in the first 90 min (Fig. 7B), with originated intermediate products absorbing in the UV region i.e. from 200 nm to 250 nm. Due to an intense peak (Fig. 7A), the RhB dye depletion followed the IC removal, but at slightly lower kinetics. Actually, the calculated K_{app} was 1.05 x 10^{-2} min^{-1} and 1.21 x 10^{-2} min^{-1} in case of RhB and IC, respectively. The degradation kinetics of RhB was also found lower compared to when it was tested alone (K_{app} 1.57 x 10^{-2} min^{-1}) (Fig. 7C). This decrease in RhB removal kinetics probably was due to the limited ROS availability for the attack and degradation of both dyes. The investigation revealed that both dyes underwent simultaneous degradation with the formation of IC dye intermediates products probably because of the good interaction of both dyes enabled by the membrane, in contrast to our previously reported observation with the dispersed α/β-Bi_2O_3 nanoparticles, where the IC was preferentially degraded, and after its complete degradation, the activity was directed against RhB [42].

View Article Online
DOI: 10.1039/D0EN01026J

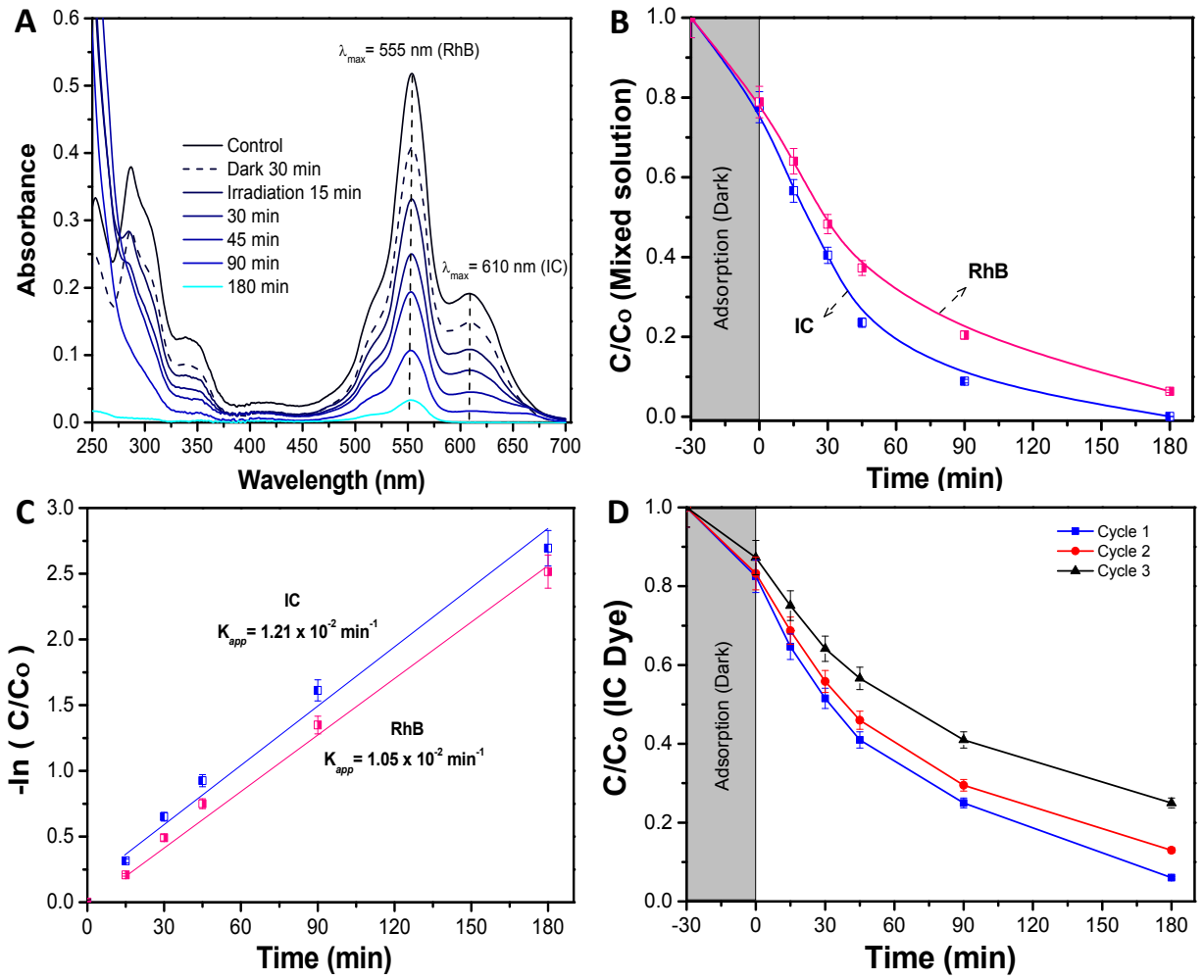

Figure 7 A) Absorbance spectra vs irradiation time of the mixed solution B) relative concentration (C/Co) of combined dyes degradation using Bi_2O_3/Nylon composite, C) Kinetic curves of removal of IC and RhB dyes in the mixed solution, and estimated K_{app}. D) Cyclic stability of Bi_2O_3/Nylon composite membrane up to three cycles; C/C_o profiles at 5 ppm IC dye concentration.

Here the equal and concurrent interaction of both dyes with the originated ROS is supported by the membrane. The overall obtained results suggested no/less interfering behavior among the tested dyes, as the removal kinetics of both dyes was almost similar i.e. from 1.21×10^{-2} min^{-1} and 1.05×10^{-2} min^{-1}, for IC and RhB, respectively.

3.2.5 Cyclic stability

View Article Online
DOI: 10.1039/D0EN01026J

For the cyclic stability of the Bi_2O_3/Nylon nanocomposite membrane, the photocatalytic tests were carried out up to three cycles i.e. after the composite membrane was recovered and rinsed and configured again in the CPMR. Fig. 7D shows the relative concentration (C/C_o) decrease of the IC dye at 5 ppm concentration up to three cycles. The composite membrane showed good stability and performance in the first two cycles; however, the removal efficiency significantly decreased in the third cycle. This reduction could be associated with membrane exhaustion due to an altered porosity or to the affected active sites of the Nylon fibers, and integrated α/β-Bi_2O_3 particles that previously had sustained the capture of dye molecules and intense interaction with the originated radical species.

3.3 Antibacterial Activity

3.3.1 Bacterial inhibition on solid media

The main aim of this study was to evaluate the potential of the composite membrane for the photocatalytic inactivation of waterborne pathogens i.e. *E. coli*. Therefore, initially, the inhibition tests were performed on *E. coli* cultured on solid media. The obtained results, showed in Fig. 8A, confirmed a growth inhibition halo against *E. coli* in the case of the composite membrane compared to the bare Nylon membrane and control samples (biotic control). The calculated zone of inhibition was around 14 mm. Moreover, under dark conditions, no significant inhibition zone was observed in the case of the composite membrane, revealing that the integrated α/β-Bi_2O_3 particles remained inactive and did not generate ROS against the growth of *E. coli*. Only a little zone of inhibition was recorded in some replicates, highlighting that probably the integrated α/β-Bi_2O_3 particles at high concentration can be a little bit toxic against the bacterial growth, too. While in the case of bare Nylon and control samples (without membranes), a high growth of *E. coli* was

View Article Online
DOI: 10.1039/D0EN01026J

observed in the whole petri dish, both under dark and irradiated conditions, resulting in no significant effect on the bacterial growth.

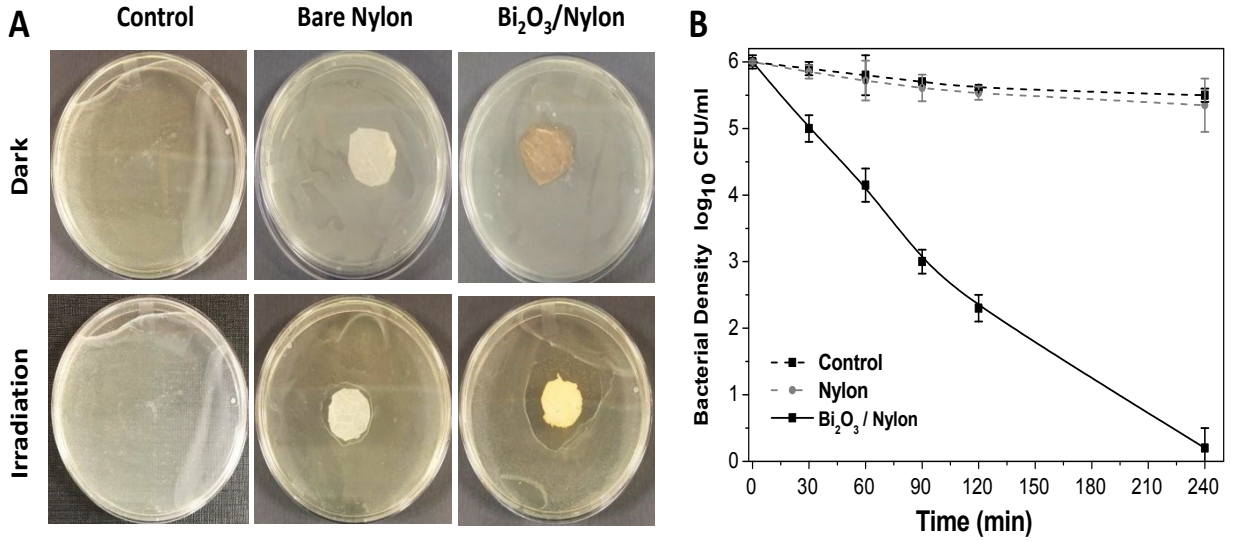

Figure 8 A) Bacterial inhibition on solid media of control, bare Nylon, and Bi_2O_3/Nylon after incubation in the dark or under LED irradiance; B) E. coli density reduction in a liquid suspension treated with the photocatalytic Bi_2O_3/Nylon membrane.

3.3.2 Bacterial inhibition in liquid suspension

Once the antibacterial activity of the composite membrane was assessed on solid agar media, the photocatalytic response against a liquid stock solution of *E. coli* at a concentration of $1x10^6$ CFU/mL was evaluated by using the CPMR. The obtained results revealed a continuous *E. coli* reduction during the photocatalytic exposure i.e. as shown in Fig. 8B. The number of bacterial cells assessed by the plate count method of serially diluted samples collected from the CPMR at specified times confirmed the reduction of the cell density. It revealed a 50% of log reduction of *E. coli* after 90 min, and their complete removal after 240 min of treatment (as observed in Fig. 8B). To further confirm that the composite membrane has a biocidal effect on the microorganisms, the fluorescence live/dead cell staining and imaging were applied i.e. using fluorescence microscopy. The samples were taken from the CPMR and stained, resulting in green-stained cells

View Article Online
DOI: 10.1039/D0EN01026J

that represent living bacteria, whereas the red-stained cells are dead. The acquired fluorescence microscopy images of *E. coli* are shown in Fig. 9. In the beginning, plenty of live green-stained cells were observed, while at continued photocatalytic exposure, the red-stained cell increased their number. The obtained fluorescence images revealed that the bacterial cells were attacked by the α/β-Bi_2O_3 in the composite membrane, resulting in the rupture of their cell membranes and allowing the PI dye to stain the DNA inside the nucleus, as indicated from the observed red-stained cells. After treatment of 240 min, a higher proportion of red-stained cells over green-stained cells revealed that the Bi_2O_3/Nylon composite membrane has not only a biostatic effect (growth inhibition) on the treated *E. coli* cells, but it acts as a biocidal material, able to kill this bacterial strain. During the photocatalytic reaction, the catalytic material integrated into the membranes could produce ROS that could attack the bacterial cell, lead to cell damage, and increase the permeability of the cell membrane towards PI staining dye [63]. Compared to these results, the bare Nylon and control samples showed no significant red stained (dead) cells after prolonged exposure; the acquired fluorescence images for bare Nylon treatment and control (without any membrane) samples are given in supplementary data Fig. S4.

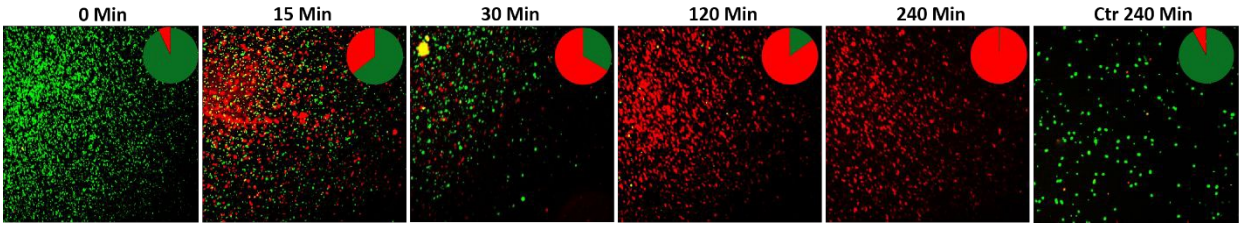

Figure 9 Fluorescence stained images of live and dead E. coli cells at different treatment time

3.4 Photocatalytic mechanism

The photocatalytic particles partially embedded in polymeric/ceramic membranes remained active under irradiation and released reactive oxidative species (ROS) in water media and across the

View Article Online
DOI: 10.1039/D0EN01026J

adsorbed/retained pollutants [61, 64]. The dispersion of ROS across the membrane could get affected by mass-transfer limitations. However, due to the large surface created by the multi-layered nylon membrane and the exposed appearance of α/β-Bi_2O_3 particles on these layers, the large release of ROS could have been enough to reach the nearest adsorbed/retained pollutants, resulting in the dyes degradation and bacterial inactivation, compared to bare nylon. Indeed, the obtained results suggest that the α/β-Bi_2O_3 nanocomposite membranes have good adsorption assisted photocatalytic properties against the removal of both anionic and cationic dyes as well as bacteria. Some of the reported studies suggested the ROS generation around the surface of heterojunctioned α/β-Bi_2O_3 [42] and nancomposite materials i.e. Sb_2WO_6/BiOBr and $BiSbO_4$/BiOBr [38, 39]. In the case of dyes, there could be various possibilities of their interaction with the generated ROS on the α/β-Bi_2O_3 active sites of composite membrane. Either the dye molecules of IC and RhB could have been adsorbed through ionic interaction i.e., in case of IC dye via sulphonic branched groups, while for RhB dye via the carboxylic group, or the dye molecules of IC and RhB were captured within the membrane pores of the multilayered Nylon fibers. However, the good affinity of both dyes towards the composite membrane could be driven by both mechanisms i.e. through simultaneous ionic interaction and capture of dye molecules. After irradiation with visible light, the α/β-Bi_2O_3 particles in the composite membranes originated reactive species that attacked the captured/adsorbed dye molecules, performing the adsorption-assisted photocatalysis. During the photo discoloration of IC, the reactive species attacked the sulfonic groups, partially mineralized, and degraded into intermediate compounds identified as *Isatin sulfonic acid* and *2-amine-5-sulfo-benzoic acid* [65]. Instead, the degradation of RhB followed carboxylic path oxidation and reduction, resulting partly mineralized without any apparent shift of the absorbance in the UV-Vis spectrum, typical of a de-ethylation (see Fig. S3 in

View Article Online
DOI: 10.1039/D0EN01026J

supplementary data) [42]. In the case of the mixed solution, both dyes showed a good interaction and removal kinetics without any ionic inhibition/interference because of the equivalent interface provided by the membrane multilayers. Further, under prolonged exposure, the simultaneous degradation of both dyes occurred, due to the attack of ROS towards the IC and RhB dye molecules.

Concerning bacteria, the results obtained with *E. coli* revealed that probably the bacterial cells interacted with the composited α/β-Bi_2O_3 particles through multilayered channels, and were subsequently attacked by the originated ROS with resulting damage of cell wall/membrane and their constituents. It is well-known that ROS can oxidise proteins, lipids and phospholipids [66], damaging the membrane itself or simply its lipid bilayer organization, eventually leading to efflux of cytosolic contents or to cell lysis. These effects are particularly efficient on bacteria, fungi, and viruses, including multidrug-resistant strains, and due to their quick action, ROS are considered potent antimicrobial agents [67]. Similar mechanisms have been suggested for other antimicrobial metal and metal oxides, such as silver or copper, and are consistent with previous works that report the efficacy of β-Bi_2O_3 on *E. coli* and *S. aureus* [68, 69]. The adsorption of the bacterial cells in the porous structure of the composite membranes combined with the action of the bismuth-based nanomaterial irradiated with the LED visible light, allowed a complete degradation of the pathogens. Indeed, the ROS generated by the photocatalytic action of the α/β-Bi_2O_3 activated particles are more effective in the close vicinity, due to their extremely low half-life. The increased number of red-stained (dead) cells at increased photocatalytic exposure showed that live cells interacted and were attacked continuously by the photo-originated ROS. All of these results proved the potential applicability of the bismuth-based composite membranes for water treatment and sanitation.

View Article Online
DOI: 10.1039/D0EN01026J

4. Conclusion

The α/β-Bi_2O_3 powder semiconductor was synthesized by the thermal annealing of $Bi(NO_3)_3$:$5H_2O$ salt. The synthesized powder was integrated into the Nylon-6 multilayered fibrous membrane via electrospraying, and characterized by XRD, FESEM, EDX, UV-Vis, FT-IR and Raman analyses. The Bi_2O_3/Nylon nanocomposite membrane showed a photocatalytic response against the separate solution of IC and RhB dyes, with a complete discoloration. The TOC analyses revealed the partial mineralization and degradation of IC and RhB treated solutions with the formation of stable and persistent intermediates. Further, in the case of the mixed solution of IC and RhB dyes, the composite membrane showed simultaneous degradation response to anionic IC dye and cationic RhB dye, due to their equal interaction with the reactive species, originated by α/β-Bi_2O_3. Moreover, dealing with a higher concentration of IC, the degradation kinetics was reduced by 3-fold, mainly due to the high saturation of the membrane layers by the dye-intermediates.

Furthermore, the composite membrane showed an antibacterial response against *E. coli* solid and liquid cultures. In the case of solid *E. coli* media, the formation of a 14 mm inhibition zone was obtained, whereas, for liquid *E. coli* suspension ($1x10^6$ CFU/mL), the complete inhibition of bacterial growth was attained after 240 min of photocatalytic exposure. The induced bactericidal effect on *E. coli* was observed by fluorescence microscopy that confirmed the high proportion of dead over live cells. Further, the successive recycle tests employing the used membrane suggested the suitable applications and efficacy of the Bi_2O_3/Nylon nanocomposite membrane for the removal of organic dyes and inactivation of waterborne pathogens.

References

[1] S.S.C. Aiyera, T. KC, P.K. BGA, A review of solar photocatalytic degradation of wastewater using advanced oxidation processes, I Control Pollution, 31 (2015).

View Article Online
DOI: 10.1039/D0EN01026J

[2] S. Natarajan, H.C. Bajaj, R.J. Tayade, Recent advances based on the synergetic effect of adsorption for removal of dyes from waste water using photocatalytic process, Journal of Environmental Sciences, 65 (2018) 201-222.
[3] H. Dong, G. Zeng, L. Tang, C. Fan, C. Zhang, X. He, Y. He, An overview on limitations of TiO2-based particles for photocatalytic degradation of organic pollutants and the corresponding countermeasures, Water research, 79 (2015) 128-146.
[4] C.L. Bianchi, E. Colombo, S. Gatto, M. Stucchi, G. Cerrato, S. Morandi, V. Capucci, Photocatalytic degradation of dyes in water with micro-sized TiO2 as powder or coated on porcelain-grès tiles, Journal of Photochemistry and Photobiology A: Chemistry, 280 (2014) 27-31.
[5] T.A. Gadhi, L.S. Gómez-Velázquez, M. Bizarro, A. Hernández-Gordillo, A. Tagliaferro, S.E. Rodil, Evaluation of the photodiscoloration efficiency of β-Bi2O3 films deposited on different substrates by pneumatic spray pyrolysis, Thin Solid Films, 638 (2017) 119-126.
[6] C. Minero, D. Vione, A quantitative evalution of the photocatalytic performance of TiO2 slurries, Applied Catalysis B: Environmental, 67 (2006) 257-269.
[7] Y. Boyjoo, H. Sun, J. Liu, V.K. Pareek, S. Wang, A review on photocatalysis for air treatment: from catalyst development to reactor design, Chemical Engineering Journal, 310 (2017) 537-559.
[8] K. Fujiwara, Y. Kuwahara, Y. Sumida, H. Yamashita, Fabrication of photocatalytic paper using TiO2 nanoparticles confined in hollow silica capsules, Langmuir, 33 (2017) 288-295.
[9] G.R.M. Echavia, F. Matzusawa, N. Negishi, Photocatalytic degradation of organophosphate and phosphonoglycine pesticides using TiO2 immobilized on silica gel, Chemosphere, 76 (2009) 595-600.
[10] T. Hirai, Y. Bando, I. Komasawa, Immobilization of CdS nanoparticles formed in reverse micelles onto alumina particles and their photocatalytic properties, The Journal of Physical Chemistry B, 106 (2002) 8967-8970.
[11] B. Gao, P.S. Yap, T.M. Lim, T.-T. Lim, Adsorption-photocatalytic degradation of Acid Red 88 by supported TiO2: Effect of activated carbon support and aqueous anions, Chemical Engineering Journal, 171 (2011) 1098-1107.
[12] X. Wang, Y. Liu, Z. Hu, Y. Chen, W. Liu, G. Zhao, Degradation of methyl orange by composite photocatalysts nano-TiO2 immobilized on activated carbons of different porosities, Journal of Hazardous Materials, 169 (2009) 1061-1067.
[13] J.C. Joo, C.H. Ahn, D.G. Jang, Y.H. Yoon, J.K. Kim, L. Campos, H. Ahn, Photocatalytic degradation of trichloroethylene in aqueous phase using nano-ZNO/Laponite composites, Journal of hazardous materials, 263 (2013) 569-574.
[14] H. Khalilian, M. Behpour, V. Atouf, S.N. Hosseini, Immobilization of S, N-codoped TiO2 nanoparticles on glass beads for photocatalytic degradation of methyl orange by fixed bed photoreactor under visible and sunlight irradiation, Solar Energy, 112 (2015) 239-245.
[15] M. Borges, D.M. García, T. Hernández, J.C. Ruiz-Morales, P. Esparza, Supported photocatalyst for removal of emerging contaminants from wastewater in a continuous packed-bed photoreactor configuration, Catalysts, 5 (2015) 77-87.
[16] A.S. El-Kalliny, S.F. Ahmed, L.C. Rietveld, P.W. Appel, Immobilized photocatalyst on stainless steel woven meshes assuring efficient light distribution in a solar reactor, Drinking Water Engineering & Science, 7 (2014).
[17] D. Pérez-Mezcua, I. Bretos, R. Jiménez, J. Ricote, R.J. Jiménez-Rioboó, C.G. Da Silva, D. Chateigner, L. Fuentes-Cobas, R. Sirera, M.L. Calzada, Photochemical solution processing of films of metastable phases for flexible devices: the β-Bi2O3 polymorph, Scientific reports, 6 (2016) 39561.
[18] H. Dong, G. Zeng, L. Tang, C. Fan, C. Zhang, X. He, Y. He, An overview on limitations of TiO 2-based particles for photocatalytic degradation of organic pollutants and the corresponding countermeasures, water research, 79 (2015) 128-146.

View Article Online
DOI: 10.1039/D0EN01026J

[19] U.I. Gaya, A.H. Abdullah, Heterogeneous photocatalytic degradation of organic contaminants over titanium dioxide: A review of fundamentals, progress and problems, Journal of Photochemistry and Photobiology C: Photochemistry Reviews, 9 (2008) 1-12.
[20] J.M. Arsuaga, A. Sotto, G. del Rosario, A. Martínez, S. Molina, S.B. Teli, J. de Abajo, Influence of the type, size, and distribution of metal oxide particles on the properties of nanocomposite ultrafiltration membranes, Journal of membrane science, 428 (2013) 131-141.
[21] J. García-Ivars, M.-J. Corbatón-Báguena, M.-I. Iborra-Clar, Development of mixed matrix membranes: Incorporation of metal nanoparticles in polymeric membranes, in: Nanoscale Materials in Water Purification, Elsevier, 2019, pp. 153-178.
[22] Z. Xu, T. Wu, J. Shi, K. Teng, W. Wang, M. Ma, J. Li, X. Qian, C. Li, J. Fan, Photocatalytic antifouling PVDF ultrafiltration membranes based on synergy of graphene oxide and TiO2 for water treatment, Journal of Membrane Science, 520 (2016) 281-293.
[23] H. Ngang, B. Ooi, A. Ahmad, S. Lai, Preparation of PVDF–TiO2 mixed-matrix membrane and its evaluation on dye adsorption and UV-cleaning properties, Chemical engineering journal, 197 (2012) 359-367.
[24] P. Argurio, E. Fontananova, R. Molinari, E. Drioli, Photocatalytic membranes in photocatalytic membrane reactors, Processes, 6 (2018) 162.
[25] K. Zarrini, A.A. Rahimi, F. Alihosseini, H. Fashandi, Highly efficient dye adsorbent based on polyaniline-coated nylon-6 nanofibers, Journal of cleaner production, 142 (2017) 3645-3654.
[26] U.A. Qureshi, Z. Khatri, F. Ahmed, A.S. Ibupoto, M. Khatri, F.K. Mahar, R.Z. Brohi, I.S. Kim, Highly efficient and robust electrospun nanofibers for selective removal of acid dye, Journal of Molecular Liquids, 244 (2017) 478-488.
[27] H.R. Pant, M.P. Bajgai, K.T. Nam, Y.A. Seo, D.R. Pandeya, S.T. Hong, H.Y. Kim, Electrospun nylon-6 spider-net like nanofiber mat containing TiO2 nanoparticles: a multifunctional nanocomposite textile material, Journal of hazardous materials, 185 (2011) 124-130.
[28] N. Beyth, Y. Houri-Haddad, A. Domb, W. Khan, R. Hazan, Alternative antimicrobial approach: nano-antimicrobial materials, Evidence-based complementary and alternative medicine, 2015 (2015).
[29] L.Y. Ng, A.W. Mohammad, C.P. Leo, N. Hilal, Polymeric membranes incorporated with metal/metal oxide nanoparticles: a comprehensive review, Desalination, 308 (2013) 15-33.
[30] S.R. Lakhotia, M. Mukhopadhyay, P. Kumari, Cerium oxide nanoparticles embedded thin-film nanocomposite nanofiltration membrane for water treatment, Scientific reports, 8 (2018) 1-10.
[31] J. Wang, W. Liu, H. Li, H. Wang, Z. Wang, W. Zhou, H. Liu, Preparation of cellulose fiber–TiO2 nanobelt–silver nanoparticle hierarchically structured hybrid paper and its photocatalytic and antibacterial properties, Chemical engineering journal, 228 (2013) 272-280.
[32] A.F. de Faria, A.C.M. de Moraes, P.F. Andrade, D.S. da Silva, M. do Carmo Gonçalves, O.L. Alves, Cellulose acetate membrane embedded with graphene oxide-silver nanocomposites and its ability to suppress microbial proliferation, Cellulose, 24 (2017) 781-796.
[33] M. Zahid, E.L. Papadopoulou, G. Suarato, V.D. Binas, G. Kiriakidis, I. Gounaki, O. Moira, D. Venieri, I.S. Bayer, A. Athanassiou, Fabrication of visible light-induced antibacterial and self-cleaning cotton fabrics using manganese doped TiO2 nanoparticles, ACS Applied Bio Materials, 1 (2018) 1154-1164.
[34] M. Ou, S. Wan, Q. Zhong, S. Zhang, Y. Song, L. Guo, W. Cai, Y. Xu, Hierarchical Z-scheme photocatalyst of g-C3N4@ Ag/BiVO4 (040) with enhanced visible-light-induced photocatalytic oxidation performance, Applied Catalysis B: Environmental, 221 (2018) 97-107.
[35] Z. Ai, Y. Huang, S. Lee, L. Zhang, Monoclinic α-Bi2O3 photocatalyst for efficient removal of gaseous NO and HCHO under visible light irradiation, Journal of Alloys and Compounds, 509 (2011) 2044-2049.
[36] Y. Sun, W. Wang, L. Zhang, Z. Zhang, Design and controllable synthesis of α-/γ-Bi2O3 homojunction with synergetic effect on photocatalytic activity, Chemical engineering journal, 211 (2012) 161-167.

View Article Online
DOI: 10.1039/D0EN01026J

[37] M. Jia, X. Hu, S. Wang, Y. Huang, L. Song, Photocatalytic properties of hierarchical BiOXs obtained via an ethanol-assisted solvothermal process, Journal of Environmental Sciences, 35 (2015) 172-180.
[38] Y. Wang, K. Wang, J. Wang, X. Wu, G. Zhang, Sb2WO6/BiOBr 2D nanocomposite S-scheme photocatalyst for NO removal, Journal of Materials Science & Technology, (2020).
[39] Z. Wang, K. Wang, Y. Li, L. Jiang, G. Zhang, Novel BiSbO4/BiOBr nanoarchitecture with enhanced visible-light driven photocatalytic performance: oxygen-induced pathway of activation and mechanism unveiling, Applied Surface Science, 498 (2019) 143850.
[40] S. Sood, A. Umar, S.K. Mehta, S.K. Kansal, α-Bi2O3 nanorods: an efficient sunlight active photocatalyst for degradation of Rhodamine B and 2, 4, 6-trichlorophenol, Ceramics International, 41 (2015) 3355-3364.
[41] X. Meng, Z. Zhang, Bismuth-based photocatalytic semiconductors: introduction, challenges and possible approaches, Journal of Molecular Catalysis A: Chemical, 423 (2016) 533-549.
[42] T.A. Gadhi, A. Hernández-Gordillo, M. Bizarro, P. Jagdale, A. Tagliaferro, S.E. Rodil, Efficient α/β-Bi2O3 composite for the sequential photodegradation of two-dyes mixture, Ceramics International, 42 (2016) 13065-13073.
[43] M.H. El-Newehy, S.S. Al-Deyab, E.-R. Kenawy, A. Abdel-Megeed, Nanospider technology for the production of nylon-6 nanofibers for biomedical applications, Journal of Nanomaterials, 2011 (2011).
[44] A. Hernández-Gordillo, M. Bizarro, T.A. Gadhi, A. Martínez, A. Tagliaferro, S.E. Rodil, Good practices for reporting the photocatalytic evaluation of a visible-light active semiconductor: Bi2O3, a case study, Catalysis Science & Technology, 9 (2019) 1476-1496.
[45] J.-A. Park, K.Y. Cho, C.H. Han, A. Nam, J.-H. Kim, S.-H. Lee, J.-W. Choi, Quaternized Amphiphilic Block Copolymers/Graphene Oxide and a Poly (vinyl alcohol) Coating Layer on Graphene Oxide/Poly (vinylidene fluoride) Electrospun Nanofibers for Superhydrophilic and Antibacterial Properties, Scientific reports, 9 (2019) 1-13.
[46] A. Chiadò, L. Varani, F. Bosco, L. Marmo, Opening study on the development of a new biosensor for metal toxicity based on Pseudomonas fluorescens pyoverdine, Biosensors, 3 (2013) 385-399.
[47] B. Tomšič, B. Simončič, B. Orel, M. Žerjav, H. Schroers, A. Simončič, Z. Samardžija, Antimicrobial activity of AgCl embedded in a silica matrix on cotton fabric, Carbohydrate polymers, 75 (2009) 618-626.
[48] N. Murthy, H. Minor, Analysis of poorly crystallized polymers using resolution enhanced X-ray diffraction scans, Polymer, 36 (1995) 2499-2504.
[49] T.J. Athauda, U. Butt, R.R. Ozer, Hydrothermal growth of ZnO nanorods on electrospun polyamide nanofibers, MRS Communications, 3 (2013) 51.
[50] Y. Yu, R. Ma, S. Yan, J. Fang, Preparation of multi-layer nylon-6 nanofibrous membranes by electrospinning and hot pressing methods for dye filtration, RSC advances, 8 (2018) 12173-12178.
[51] K.-H. Lee, K.-W. Kim, A. Pesapane, H.-Y. Kim, J.F. Rabolt, Polarized FT-IR study of macroscopically oriented electrospun nylon-6 nanofibers, Macromolecules, 41 (2008) 1494-1498.
[52] E. Fatarella, D. Spinelli, M. Ruzzante, R. Pogni, Nylon 6 film and nanofiber carriers: Preparation and laccase immobilization performance, Journal of Molecular Catalysis B: Enzymatic, 102 (2014) 41-47.
[53] F. He, Z. He, J. Xie, Y. Li, IR and Raman spectra properties of Bi 2 O 3-ZnO-B 2 O 3-BaO quaternary glass system, American Journal of Analytical Chemistry, 5 (2014) 1142.
[54] A. Milani, Unpolarized and polarized Raman spectroscopy of nylon-6 polymorphs: a quantum chemical approach, The Journal of Physical Chemistry B, 119 (2015) 3868-3874.
[55] C. Menchaca, B. Manoun, G. Martínez-Barrera, V. Castaño, H. López-Valdivia, In situ high-temperature Raman study of crystalline nylon 6, 12 fibers gamma-irradiated in argon atmosphere, Journal of Physics and Chemistry of Solids, 67 (2006) 2111-2118.
[56] C.-H. Ho, C.-H. Chan, Y.-S. Huang, L.-C. Tien, L.-C. Chao, The study of optical band edge property of bismuth oxide nanowires α-Bi 2 O 3, Optics express, 21 (2013) 11965-11972.

View Article Online
DOI: 10.1039/D0EN01026J

[57] A.L. Pereira, J.A. Sans, R. Vilaplana, O. Gomis, F. Manjón, P. Rodriguez-Hernandez, A. Muñoz, C. Popescu, A. Beltrán, Isostructural second-order phase transition of β-Bi2O3 at high pressures: an experimental and theoretical study, The Journal of Physical Chemistry C, 118 (2014) 23189-23201.
[58] M.-W. Kim, B. Joshi, E. Samuel, K. Kim, Y.-I. Kim, T.-G. Kim, M.T. Swihart, S.S. Yoon, Highly nanotextured β-Bi2O3 pillars by electrostatic spray deposition as photoanodes for solar water splitting, Journal of Alloys and Compounds, 764 (2018) 881-889.
[59] M. Ghani, A.A. Gharehaghaji, M. Arami, N. Takhtkuse, B. Rezaei, Fabrication of electrospun polyamide-6/chitosan nanofibrous membrane toward anionic dyes removal, Journal of Nanotechnology, 2014 (2014).
[60] L. Aoudjit, P.M. Martins, F. Madjene, D. Petrovykh, S. Lanceros-Mendez, Photocatalytic reusable membranes for the effective degradation of tartrazine with a solar photoreactor, Journal of hazardous materials, 344 (2018) 408-416.
[61] X. Zheng, Z.-P. Shen, L. Shi, R. Cheng, D.-H. Yuan, Photocatalytic membrane reactors (PMRs) in water treatment: configurations and influencing factors, Catalysts, 7 (2017) 224.
[62] R. Halim, R. Utama, S. Cox, P. Le-Clech, Performances of submerged membrane photocatalysis reactor during treatment of humic substances, Membr. Water Treat, 1 (2010) 283-296.
[63] A. Mecha, M. Onyango, A. Ochieng, M. Momba, UV and solar photocatalytic disinfection of municipal wastewater: inactivation, reactivation and regrowth of bacterial pathogens, International journal of environmental science and technology, 16 (2019) 3687-3696.
[64] V. Melinte, L. Stroea, A.L. Chibac-Scutaru, Polymer Nanocomposites for Photocatalytic Applications, Catalysts, 9 (2019) 986.
[65] T.T. Guaraldo, T.B. Zanoni, S.I. de Torresi, V.R. Gonçales, G.J. Zocolo, D.P. Oliveira, M.V.B. Zanoni, On the application of nanostructured electrodes prepared by Ti/TiO2/WO3 “template”: A case study of removing toxicity of indigo using visible irradiation, Chemosphere, 91 (2013) 586-593.
[66] M.Y. Memar, R. Ghotaslou, M. Samiei, K. Adibkia, Antimicrobial use of reactive oxygen therapy: current insights, Infection and drug resistance, 11 (2018) 567.
[67] M. Dryden, Reactive oxygen species: a novel antimicrobial, International journal of antimicrobial agents, 51 (2018) 299-303.
[68] Y.-G. Yuan, Q.-L. Peng, S. Gurunathan, Effects of silver nanoparticles on multiple drug-resistant strains of Staphylococcus aureus and Pseudomonas aeruginosa from mastitis-infected goats: an alternative approach for antimicrobial therapy, International journal of molecular sciences, 18 (2017) 569.
[69] M.K. Ballo, S. Rtimi, S. Mancini, J. Kiwi, C. Pulgarin, J.M. Entenza, A. Bizzini, Bactericidal activity and mechanism of action of copper-sputtered flexible surfaces against multidrug-resistant pathogens, Applied microbiology and biotechnology, 100 (2016) 5945-5953.

View Article Online
DOI: 10.1039/D0EN01026J

Graphical Abstract